RESEARCH ARTICLE | MAY 10 2023

Large eddy simulation of turbulent wake flow around a marine propeller under the influence of incident waves ⊕ ✓

Special Collection: Turbulence in Plasmas and Fluids

Kan Kan (阚阚) ⓘ ; Li Haoyu (李昊宇) ⓘ ; Yang Zixuan (杨子轩) ✉ ⓘ

Check for updates

View Online   Export Citation

Large eddy simulation of turbulent wake flow around a marine propeller under the influence of incident waves EP

View Online   Export Citation   CrossMark

Kan Kan (阚阚),[1,2] Haoyu Li (李昊宇),[1] and Zixuan Yang (杨子轩)[3,4,a]

AFFILIATIONS

[1]College of Energy and Electrical Engineering, Hohai University, Nanjing 211100, People's Republic of China
[2]College of Water Conservancy and Hydropower Engineering, Hohai University, Nanjing 210098, People's Republic of China
[3]Institute of Mechanics, Chinese Academy of Sciences, Beijing 100190, People's Republic of China
[4]School of Engineering Sciences, University of Chinese Academy of Sciences, Beijing 101408, People's Republic of China

Note: This paper is part of the special topic, Turbulence in Plasmas and Fluids.
[a]Author to whom correspondence should be addressed: yangzx@imech.ac.cn

ABSTRACT

In practical applications, propellers often operate beneath incident waves. To investigate the effects of waves on turbulent propeller wakes, a comparative study of the instantaneous flow fields and turbulent statistics of propeller wakes under open-water condition and with incident waves is conducted through the large-eddy simulation framework. The simulations are performed on a Cartesian grid, with the air–water interface captured using a coupled level-set and volume-of-fluid method. The complex geometry of the propeller is captured using an immersed boundary method. The results show that, near the water surface, the existence of incident waves accelerates the wake flow in the axial direction. Both the mean axial velocity and turbulent kinetic energy exhibit phase-lag behavior in the presence of incident waves. Waves increase the instability of the flow in the far-wake region, resulting in the rising of turbulent kinetic energy. Further analysis of the power spectral density shows that the velocity fluctuations gain energy from the waves at low frequencies, and nonlinear interactions between wave-induced motion and turbulent fluctuations transport energy from low to high frequencies as the wake flows downstream. The present study shows the potential of the large-eddy simulation framework to provide engineering guidance and a theoretical basis for the design and operation of propellers in wave environments.

I. INTRODUCTION

Propellers play a crucial role in both ocean and aviation engineering. As a type of rotating machinery that provides propulsion for watercraft and aircraft, propellers are expected to remain a primary form of propulsion for the foreseeable future.[1,2] In recent years, there has been a significant increase in demand for improved propeller performance, which has led to intensive research on the complex flow phenomena associated with propellers.[3,4] These phenomena involve a range of issues, including hydrodynamics, aerodynamics, and noise acoustics. As a result, an increasing number of researchers have become interested in this area of study.[5,6]

In experimental studies for marine propellers, laser doppler velocimetry and particle image velocimetry have been used to measure the flow field around propellers.[7–9] Felli and coworkers[10–12] conducted a series of experimental studies on the wake properties of propellers.

They performed analyses of the velocity and pressure fields with phase measurements to investigate the wake development properties of a marine propeller and revealed the effect of the blade number on wake development by analyzing the correlation between the blade-to-blade velocity interaction and pressure distribution. The development mechanisms of the tip and hub vortices in both the transitional region and far field of the propeller were also reported.

With recent increases in computing power, computational fluid dynamics (CFD) has been used to study the flow around propellers.[13–15] Numerical simulations can resolve the entire flow field around the propeller with high precision.[16] Reynolds-averaged Navier–Stokes simulation (RANS) is commonly used to investigate the efficiency, loads, wake, and cavitation of propellers. Owing to the highly unsteady nature of the propeller wake, unsteady-state RANS is the primary approach for studying these characteristics.[17] For

example, Baek et al.[18] applied the shear-stress transport (SST) k–ω model to study the influence of the velocity coefficient on the evolution of propeller wakes. Heydari and Sadat-Hosseini[19] studied the wake field and vortex structures of a propeller using the same model and observed a strong correlation between the advance coefficient and the formation, trajectory, and stability of wake vortex structures. Ji et al.[20] and Long et al.[21] investigated the propeller cavitation flow by applying the SST k–ω model.

Compared with the RANS approach, the large-eddy simulation (LES) framework achieves higher fidelity in resolving the unsteady wake flow field.[22,23] LES was utilized by Hu et al.[24] to study the tip vortex of a contra-rotating propeller. Their simulations showed the feasibility of using LES to investigate unsteady flows. Kumar and Mahesh[25] discovered the wake instabilities of a propeller induced by the interaction between the tip vortex and the adjacent blade wake by conducting LES, and another instability mechanism induced by the interaction among adjacent helical vortex sheets in the transition region was proposed by Ahmed et al.[26] through the analyses of LES data. Wang et al.[27] investigated the joint effects of a leap-frogging mechanism and the interaction between the root and hub vortices that induce instabilities in the wake flow of another type of propeller, namely the contracted and load tip propeller. RANS/LES hybrid methods are also effective in studying the flow past propellers. Sun et al.[28] investigated the scale effects on the propeller wake dynamics using the detached-eddy simulation (DES), and Zhang and Jaiman[29] adopted a delayed detached-eddy simulation model (DDES) to study the wake dynamics of a ducted propeller. Wang et al.[30] studied the wake instability of propeller under heavy load by comparatively using improved delayed detached-eddy simulation (IDDES) and LES, respectively, and pointed out that LES can solve more turbulence details.

In practical applications, the operating environment of propellers is complex. As propulsion equipment, propellers often operate close to the water surface.[31] Under this condition, the influence of the water surface on the propeller cannot be ignored. Di Mascio et al.[32] compared the vortex structures in the wake of a propeller under open-water and near-surface conditions. They discovered two coexisting effects of the water surface on the vortex structures. The first was a stabilizing effect related to the relatively high velocity in the slip-stream region, and the second was a destabilizing effect associated with the loss of axial symmetry. Wang et al.[33] showed that strong fluctuations of the water surface caused wake instability, leading to the merging and breakdown of tip vortices in the near field, particularly at low advance coefficients. Paik[34] investigated the propeller performance below the water surface and demonstrated that operating near the water surface reduced the propeller efficiency. Paik[34] and Guo et al.[35] concluded that the effect of the water surface on the thrust and torque was highly dependent on the advance coefficient, submergence depth, and the size of the model propeller. Li et al.[36] found that the highest blade force loss occurred when near the apex position because of the broken symmetry caused by the water surface and that the amplitude of higher harmonics in the blade forces increased as a result.

Several scholars have studied the performance of propellers under the operation condition with incident waves. Zhao et al.[37] analyzed the unsteady hydrodynamic performance of propellers in the case of incident waves. They found that the thrust and torque of the propellers showed strong unsteady behavior when operating beneath waves. Zhang et al.[38] investigated the effect of the water surface on the

dynamic loads of a propeller in regular head waves, considering the coupling effect of an oblique flow and a free surface. They demonstrated that, under the condition of full submergence, the azimuth corresponding to the maximum thrust and torque shifts due to the inhomogeneity of the inflow. Eom et al.[39] compared the propeller performance at various immersion depths in calm water and beneath waves. They concluded that the propeller performance with respect to the wave elevation displayed a similar trend to that with respect to the immersion depth in calm water.

To the best of our knowledge, among the many studies investigating the effects of incident waves on propellers, the vast majority have focused on the performance or loads of the propeller. There have been few investigations on the turbulence properties of the propeller wake under the influence of incident waves. In fact, for propellers operated beneath incident waves, their wake can interact nonlinearly with the waves, exhibiting strong unsteady characteristics. Studying the effect of incident waves on the turbulent wake flow is of engineering significance. In this study, a sharp interface immersed boundary (IB) method is applied to capture the complex and moving boundary geometry of a marine propeller. The influence of incident waves on the propeller wake characteristics, including the turbulent kinetic energy (TKE) and power spectral density (PSD), is analyzed.

The remainder of this paper is organized as follows. In Sec. II, the numerical methodology is introduced. Section III presents the setup for the numerical simulations. In Sec. IV, the simulation results are validated and analyzed. Finally, the conclusions to this study are presented in Sec. V.

II. NUMERICAL METHODOLOGY
A. Governing equation and numerical method

A high-fidelity in-house solver known as the computational air–sea tank (CAS-tank)[40] was used to conduct the numerical simulations. The filtered continuity and momentum equation of incompressible flow are expressed as

$$\frac{\partial \tilde{u}_i}{\partial x_i} = 0, \tag{1}$$

$$\frac{\partial \tilde{u}_i}{\partial t} + \frac{\partial (\tilde{u}_i \tilde{u}_j)}{\partial x_i} = -\frac{1}{\rho}\frac{\partial \tilde{p}}{\partial x_i} + \frac{\mu}{\rho}\frac{\partial^2 \tilde{u}_i}{\partial x_j \partial x_j} - g\delta_{i2} - \frac{\partial \tau_{ij}}{\partial x_j} + f_i, \tag{2}$$

where t is the time, x_i for $i = 1, 2,$ and 3 (or x, y, and z) denotes the coordinates in the streamwise, vertical, and lateral directions, respectively, u_i defines the velocity component in the corresponding direction, the tilde $(\tilde{\cdot})$ denotes the implicit filtering operator at the grid-level size, ρ is the fluid density, p is the pressure, μ is the dynamic viscosity, g is the gravity, and δ_{ij} represents the Kronecker delta tensor. The subgrid-scale (SGS) stress tensor τ_{ij} is calculated using the dynamic Smagorinsky–Lily model[41] as

$$\tau_{ij} - \frac{1}{3}\tau_{kk}\delta_{ij} = -2\nu_t \tilde{S}_{ij}. \tag{3}$$

The eddy viscosity ν_t is calculated as

$$\nu_t = C\Delta^2 \sqrt{2\tilde{S}_{ij}\tilde{S}_{ij}}, \tag{4}$$

where C is the model coefficient, determined dynamically by the Germano identity,[42] Δ is the filtering scale, and S_{ij} is the strain-rate

tensor. Note that a negative model coefficient ($C < 0$) can cause numerical instability. Following the convention, if a negative coefficient is obtained, it is clipped to zero. The last term f_i in Eq. (2) represents the external forcing corresponding to the IB method, which is described in detail in Sec. II B.

B. Level-set based sharp-interface IB method

In the present study, we adopt a sharp-interface IB method to capture the complex geometry of the propeller. The feasibility of using the IB method for numerical simulations of turbulent flow around a propeller has been verified in many previous studies.[43–46] A level-set (LS) function ψ is used to define the IB, defined as

$$\psi(d, t) = \begin{cases} |d| & \text{in fluid domain,} \\ 0 & \text{on interface,} \\ -|d| & \text{in solid domain,} \end{cases} \quad (5)$$

where d is the distance from each grid node to the solid–fluid interface, namely the IB. From Eq. (5), it is understood that the value of ψ is positive and negative in the fluid domain and solid domain, respectively. The LS function field is obtained using a ray-tracing algorithm.[47,48]

The applied IB method is established on a staggered Cartesian grid. For low-Reynolds-number problems, the viscous sublayer near the solid boundary can be fully resolved by the grid. As such, the velocities at IB nodes can be determined by linear interpolation. In practical applications, the high-Reynolds-number effect means that the viscosity sublayer is often unresolvable. Therefore, a model needs to be applied to correct the momentum flux at the IB nodes. For this purpose, the velocity and eddy viscosity at IB nodes is reconstructed by solving the thin boundary layer equation,[49] which is expressed as

$$\frac{\partial}{\partial y}\left((\nu + \nu_t)\frac{\partial u}{\partial y}\right) = 0, \quad (6)$$

$$\frac{\nu_t}{\nu} = \kappa y^+ \left(1 - e^{-y^+/A+}\right)^2 u_\tau, y^+ = yu_\tau/\nu, \quad (7)$$

where u represents the velocity in the tangential direction of the wall, y is the wall-normal coordinate, κ is the von Kármán constant, u_τ is the friction velocity, A^+ is the damping coefficient, and y^+ is the wall-normal coordinate in wall units.

C. Interface-capturing method

The coupled level-set and volume-of-fluid (CLSVOF) method[50] is applied to capture the air–water interface. The LS and VOF functions are evolved by solving the following convection equations:

$$\frac{\partial \phi}{\partial t} + \frac{\partial(\phi u_i)}{\partial x_i} = 0, \quad (8)$$

$$\frac{\partial F}{\partial t} + \frac{\partial(F u_i)}{\partial x_i} = 0, \quad (9)$$

where ϕ and F represent the LS and VOF functions. Note that the LS function ϕ is used to capture the air–water interface and is different from the LS function ψ defined in Eq. (5) for capturing the solid body surface. To calculate the flux of the VOF function accurately, a piecewise linear calculation algorithm is used to reconstruct the interface. The LS function is used to determine the normal direction of the interface, while the distance between the interface and the cell center is
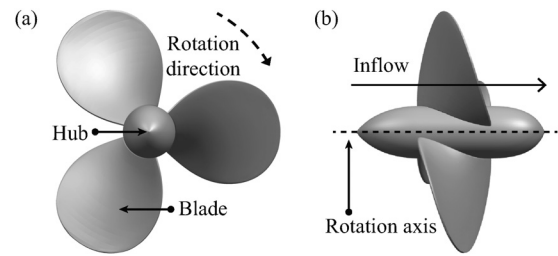

FIG. 1. Propeller model: (a) front view and (b) side view.

determined by the VOF function. After evolving the LS and VOF functions, the interface is reconstructed, and the LS function is reinitialized according to the reconstructed interface. Based on the LS function, the density and viscosity are determined as

$$\rho = \rho_a(1 - H(\phi)) + \rho_w H(\phi), \quad (10)$$

$$\mu = \mu_a(1 - H(\phi)) + \mu_w H(\phi), \quad (11)$$

$$H(\phi) = \begin{cases} 0, & \phi \leq 0, \\ 1, & \phi > 0, \end{cases} \quad (12)$$

where the subscripts "a" and "w" represent "air" and "water," respectively.

III. SIMULATION SETUP
A. Propeller model

The propeller model employed in this study, the DTMB P4119 (Ref. 51), is commonly used for validating numerical methods. Numerous experiments and simulation have been conducted using this model, providing ample data for comparison. The propeller contains a hub without a stationary shaft and three blades with no trim and a zero lateral oblique angle. The geometric model is illustrated in Fig. 1, and the specific parameters are listed in Table I.

B. Computational domain

Figure 2 shows the computational domain, which is a box with $L_1 \times L_2 \times L_3 = 8D \times 3.5D \times 3.5D$. In the streamwise direction, a periodic boundary condition is prescribed. Velocity relaxation zones are applied on two sides of the computational domain in the x-direction. The relaxation zone has a width of D and $2D$ near the upstream and downstream boundaries, respectively. As such, the inflow and outflow are stable. In particular, the velocity in the

TABLE I. Main geometric parameters of the propeller model.

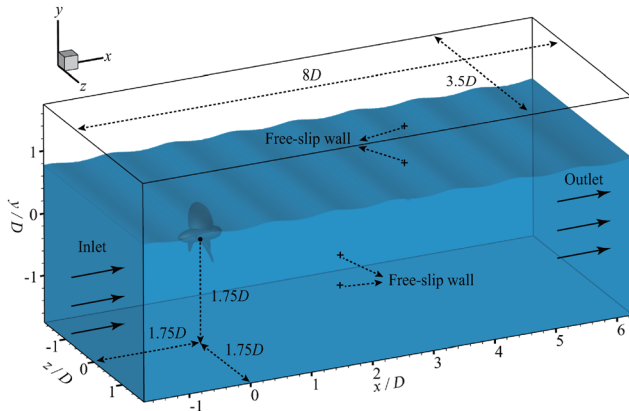| Parameter	Notation	Value
Diameter	D (m)	0.305
Blade number	Z	3
Hub diameter ratio	D_{Hub} / D	0.2
Disk ratio	A_E / A_o	0.6
Trim angle	ε (deg)	0
Lateral oblique angle	θ_S (deg)	0
Leaf profile shape	$\cdots$	NACA66-mod

FIG. 2. Computational domain.

relaxation zone is set to zero on the air side, while the target velocity on the water side is determined by the analytical solution of a third-order Stokes wave. At other boundaries, a free-slip condition is applied. The propeller is placed $1.75D$ downstream of the inlet, centered in the lateral direction.

More than 100×10^6 grid points are used to discretize the computational domain. The number of grid points is $N_1 \times N_2 \times N_3 = 920 \times 336 \times 336$. The grids are displayed in Fig. 3. To facilitate a clear illustration, only one of every four grid nodes is displayed. To ensure the resolution near the propeller blades, the grid nodes in this region are locally refined and gradually stretched to the far field. The grid resolution around the propeller is $0.006D$. For the case with incident waves, the refined region is extended in the vertical direction, and the number of grid points is correspondingly increased to ensure that the resolution-refined region covers the water surface, allowing the deformation of the air–water interface to be captured. The time step is set to 5.555×10^{-5} s, corresponding to propeller rotation by $0.2°$.

C. Operating conditions

In the present study, three different operating conditions are investigated and compared. The first is a single-phase flow without water surface, which is also known as an open-water condition. The second case is a two-phase flow with incident waves. We also introduce the third condition with a flat inflow surface into the spectral

TABLE II. Different grid configuration schemes.

Serial number	Grid scheme	Number of grid nodes N_g	Minimum grid resolution Δ_r
Grid I	$790 \times 288 \times 288$	65.5×10^6	$0.0070D$
Grid II	$850 \times 312 \times 312$	82.7×10^6	$0.0065D$
Grid III	$920 \times 336 \times 336$	103.9×10^6	$0.0060D$
Grid IV	$990 \times 360 \times 360$	128.3×10^6	$0.0055D$

analysis. For all cases, the propeller is operated under the designed condition. The advance ratio is $J = U/(nD) = 0.833$, where $U = 2.541$ m/s is the free-stream inflow velocity and $n = 600$ rpm is the rotation speed of the propeller. The Reynolds number is defined using the inflow velocity U, propeller diameter D, and kinematic viscosity of water ν_w,

$$Re = \frac{UD}{\nu_w}, \quad (13)$$

giving a value of approximately $770\,000$. For the two cases with free surface, the Froude number is defined as

$$Fr = \sqrt{\frac{U^2}{gD}}. \quad (14)$$

The wavelength and steepness of the incident waves are specified as $\lambda = D$ and $ka = 0.15$, respectively. Note that the ratio of the wavelength to the propeller size is a significant parameter that affects the interaction between the wave-induced motion and turbulent wake of the propeller. For the purpose of our investigation, we have chosen a special condition with $\lambda = D$, since this condition is likely to result in a strong nonlinear interaction when the two characteristic length scales are close to each other. The submerging depth of the propeller is set to $0.75D$. As such, the whole blade remains submerged in water, and there is no extreme situation of ventilation.

D. Validation

To determine the grid resolution, we have conducted a resolution-convergence test. The details of different grid sets are summarized in Table II. The test is conducted under the open-water condition without water surface. Table III compares the simulation results
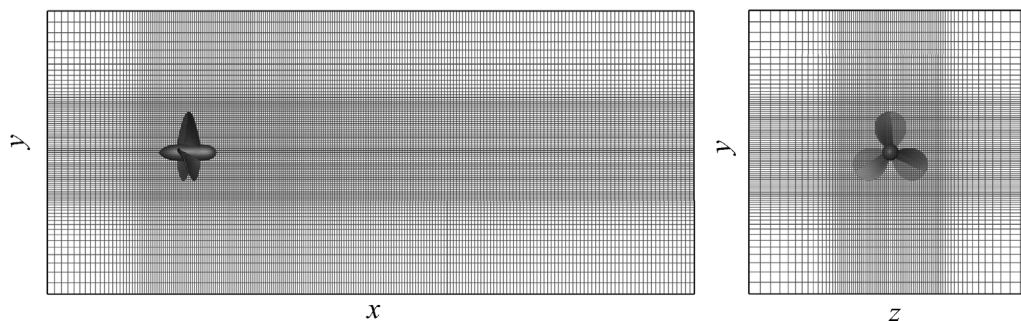

FIG. 3. Grid diagram.

TABLE III. Comparison of unsteady load coefficients among experiment and different grid schemes.

	Experiment	Grid I	Grid II	Grid III	Grid IV
K_T (relative error/%)	0.146(-)	0.1611 (+10.34)	0.1548 (+6.03)	0.1530 (+4.79)	0.1521 (+4.18)
K_Q (relative error/%)	0.028(-)	0.0317 (+13.21)	0.0299 (+6.79)	0.0292 (+4.29)	0.0291 (+3.93)

of two fundamental indices of propeller performance, namely the thrust coefficient K_T and torque coefficient K_Q, using different grid resolutions. Here, K_T and K_Q are defined as

$$K_T = \frac{T}{\rho \cdot n^2 \cdot D^4}, \quad K_Q = \frac{Q}{\rho \cdot n^2 \cdot D^5}, \quad (15)$$

where T and Q denote the thrust and torque, respectively. The experimental results[52] are also listed for comparison. It is seen that as the number of grid points increases from Grid I to Grid III, the relative error of LES with respect to the experimental data decreases. However, as the grid resolution is further refined from $0.0060D$ to $0.0055D$, the changes in the thrust and torque coefficients become less significant. In consideration of the balance between numerical accuracy and computational costs, Grid III is ultimately chosen for running other cases with different operation conditions.

The axial–radial–circumferential $(x–r–\theta)$ coordinates used for data analysis in this paper are illustrated schematically in Fig. 4, where the origin is located at the center of the propeller blade. Figure 5 compares the circumferential-averaged axial velocity along the radial direction at two cross-stream sections obtained from the present simulations with previous experimental results.[52] It is seen that the agreement of the LES results with the experimental data is generally reasonable. At both cross-stream sections, the variation trend of the axial velocity along the radial direction is consistent with the experimental values. The maximum relative error appears at the tip $r/R = 1.0$ at both cross-stream sections, which is 9.08% and 7.63% at $x/R = 0.328$ and $x/R = 0.951$, respectively. The errors at other radial locations are mostly less than 3%.

To further validate the numerical method, we now examine the phase-averaged velocity. A total of 12 rotation periods, that is, 36 phases, are used for averaging. Figures 6 and 7 show the contours of the phase-averaged axial velocity on the central longitudinal plane and
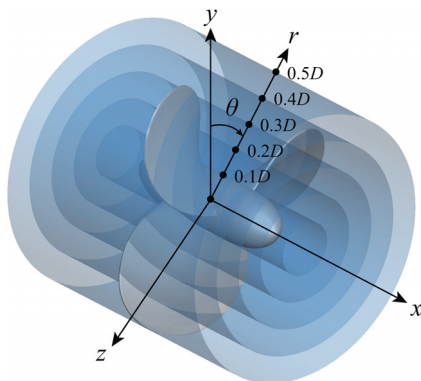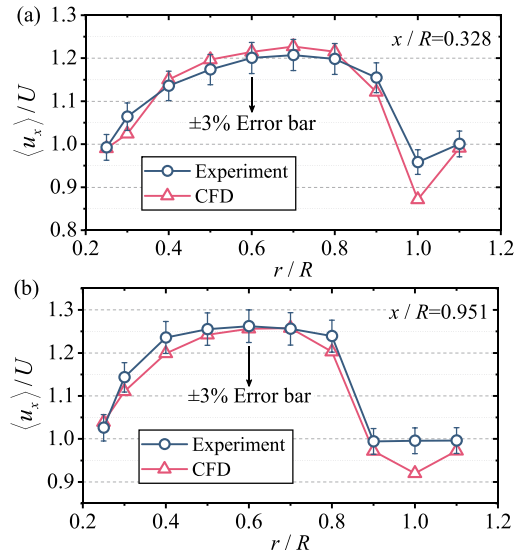

FIG. 5. Circumferential-averaged axial wake velocity of the propeller operated under the open-water condition obtained from the present simulations and experiments. The axial locations are (a) $x/R = 0.328$ and (b) $x/R = 0.951$.

various axial sections,[16] respectively. Due to the propeller rotation, the upstream and downstream fluids are accelerated, forming high-speed zones that are distributed periodically in different phases. The velocity of the wake flow is higher than that of the free stream, except in the downstream regions close to the blade tip, blade root, and hub. These downstream low-speed regions are caused by tip, root, and hub vortices in the wake, respectively. In Fig. 6, a slip-stream contraction phenomenon appears in the near-wake region. After passing through the propeller disk, the high-speed zone first experiences a contraction toward the center as the flow moves downstream. From $2D$
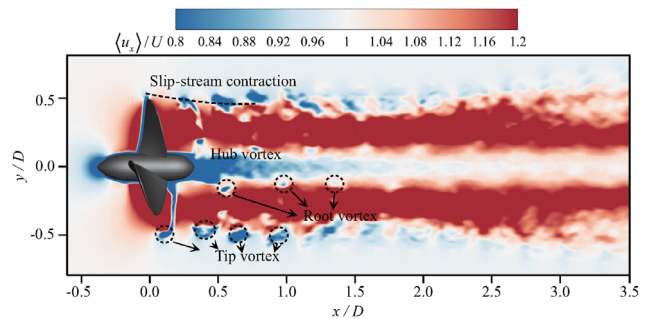

FIG. 4. Sketch of the axial–radial–circumferential $(x–r–\theta)$ coordinates used for data analyses.

FIG. 6. Phase-averaged axial wake velocity of the propeller operated under the open-water condition on the central $x–y$ plane.

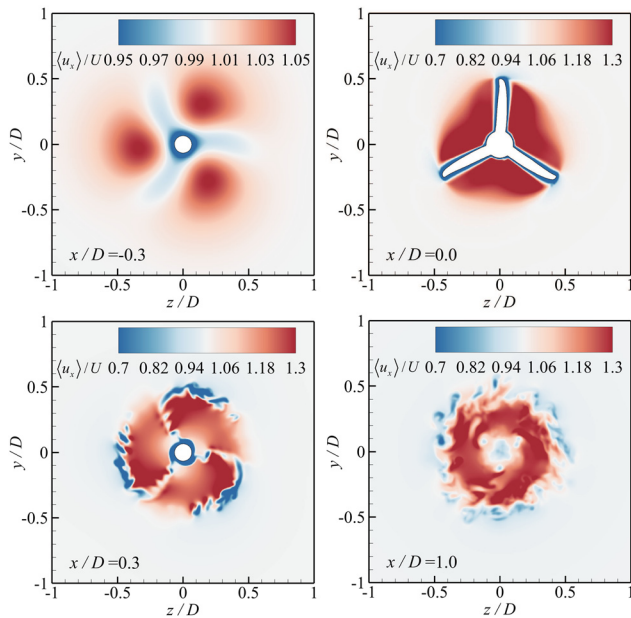**FIG. 7.** Phase-averaged axial wake velocity of the propeller operated under the open-water condition at different axial sections.

FIG. 9. Contours of instantaneous water elevation $h - h_{in}$ for the case with incident waves.

downstream of the propeller, the high-speed wake diverges, occupying an increasing area as the flow continues to move downstream, an observation that is similar to the LES results of Ahmed et al.[26] Following Ref. 26, the wake within $2D$ downstream of the propeller center is defined as the near wake, and the remaining region where the wake turns to diverge is defined as the far wake.

The above examination of the simulation results of the case under open-water condition verifies the feasibility of applying the IB method and LES to study the wake flows of propellers. In the following, we focus on the influence of incident waves on the wake flow by comparing the simulation results of cases in the environment of open-water and incident waves.

IV. RESULTS

Before conducting a quantitative analysis of the turbulence statistics, the flow features are qualitatively illustrated through the vortex
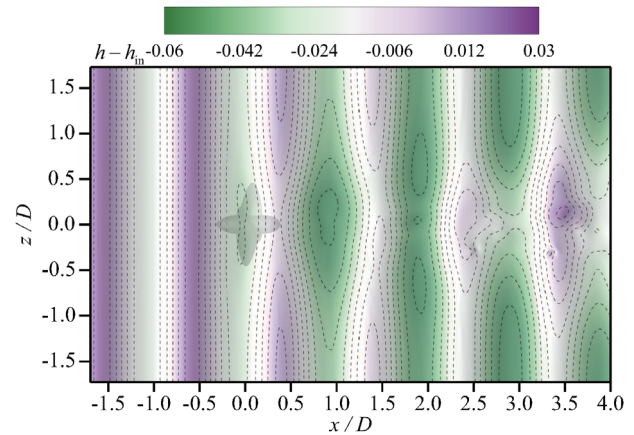
structures and wave surfaces in Figs. 8 and 9, respectively. The vortex structures are visualized using the isosurface of the Q-criterion,[53] which is defined as

$$Q_v = \frac{1}{2}(\|\Omega_{ij}\|_F^2 + \|S_{ij}\|_F^2), \quad (16)$$

where Ω_{ij} is the vorticity tensor. Figure 8 shows that spiral vortex structures are formed at the tip of the propeller. The vortices are destabilized downstream and break into smaller vortex structures due to the disturbance of the turbulent motions in the wake. At further downstream locations, the wave surface is disturbed by the propeller wake. This disturbance signal is stronger at downstream locations. As shown in Fig. 9, the propeller hardly affects the elevation of water surface in the upstream. The disturbance of the propeller to the water surface starts from $x = 0$. The water elevation above the wake flow decreases slightly due to the low-pressure behind the propeller, and this descent effect expands in the spanwise direction as the flow moves downstream.

Figure 10 compares the vertical profiles of phase-averaged axial velocity at the central span of the propeller for cases under open-water condition and with incident waves. As shown in Fig. 10(a), the middle-part of axial velocity in the near-wake region is highly
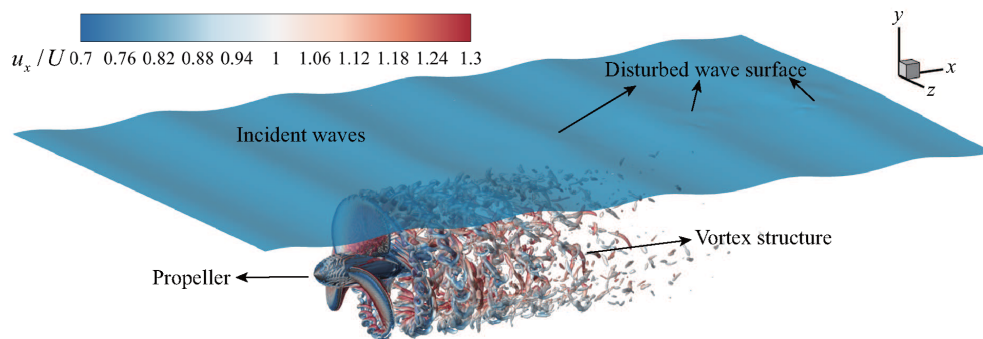

FIG. 8. Instantaneous vortex structures visualized using the iso-surface of $Q_v D^2 / U^2 = 40$ for the case with incident waves. The vortices are colored by the axial velocity.
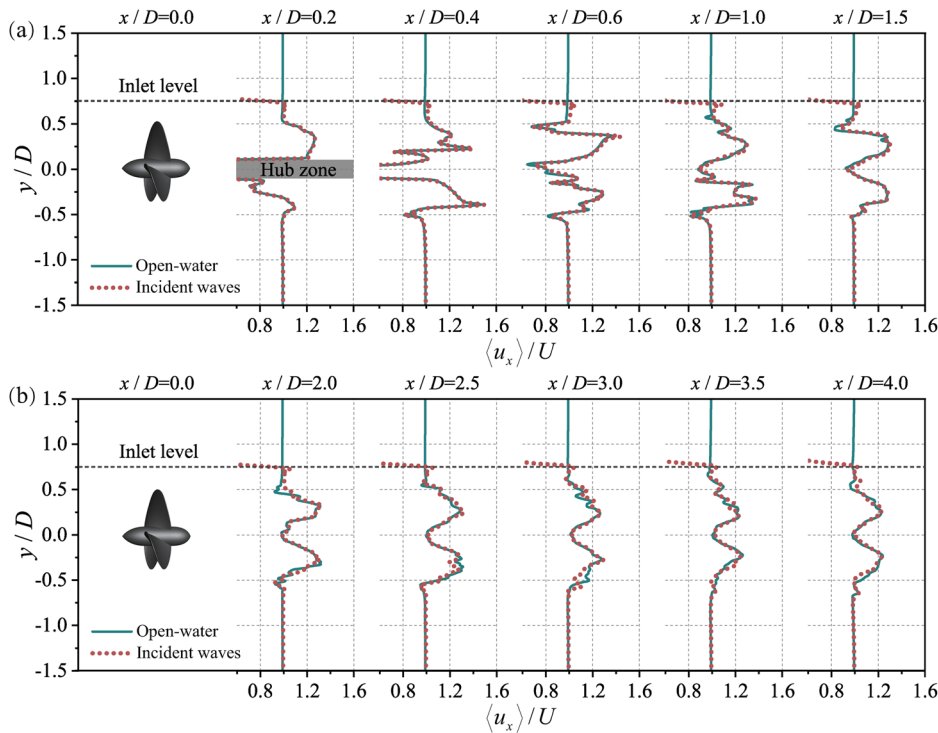
FIG. 10. Vertical profiles of phase-averaged axial velocity in the (a) near-wake region and (b) far-wake region at the central span of the propeller for cases under open-water condition and with incident waves.

consistent in the two cases. This observation indicates that the water surface imposes little influence on the near-wake of the mainstream region of the propeller. At $x/D = 0.2$, the gray shadow represents the solid domain of the hub. At $x/D = 0.4$, the flow is immediately behind the hub, where the velocity is relatively low due to blockage effect of the hub. To keep the velocity scale consistent with other locations, the velocity less than $0.8U$ is clipped in the figure. Figure 10(b) shows that, in the far-wake region, the axial velocity gradually becomes symmetric along the centerline, indicating that the wake flow is fully developed. The velocities near the water surface under the case with incident waves are different from the open-water condition in both the near-wake region and the far-wake region.

To clarify the influence of surface waves on the mean axial velocity, we compare the variation in velocity along the axial direction for two cases in Fig. 11. The results are shown at the central span of the propeller and at two different elevations, i.e., $y/D = \pm 0.55$. From Fig. 11(a), in the near-wake region, the wave effect accelerates the axial velocity and shifts the velocity phase downstream at $y/D = 0.55$. The wave effect does not reach a deeper location in the near-wake region. As a result, the mean velocity exhibits almost no difference in the two cases for $x/D < 2.0$ in Fig. 11(b). The above observations, including the phase-lag phenomenon above the propeller, were also reported by Di Mascio et al.[32] in their study of the turbulent wake of a propeller operated under a flat inflow surface at a high advance coefficient. The mechanism underlying the phase-lag phenomenon of the mean axial velocity above the propeller is not conclusive in the literature. Here, we attempt to provide a plausible explanation. When the free surface is present, the high-velocity slip-stream region generates low pressure and causes the decrease in the water elevation over the propeller. As such, the cross section area is reduced, which further leads to the

acceleration of the axial velocity because of mass conservation. As a result, the convection velocity above the propeller is slightly higher than that in an open-water environment. This results in the phase-lag behavior as shown in Fig. 11(a). In the far-wake region, the effect of incident waves reach a larger water depth. As shown in Fig. 11(b), the velocity at $y/D = -0.55$ also shows difference between the two cases.

Figure 12 compares the TKE along the axial direction at $y/D = \pm 0.55$ and at the central span of the propeller for cases under
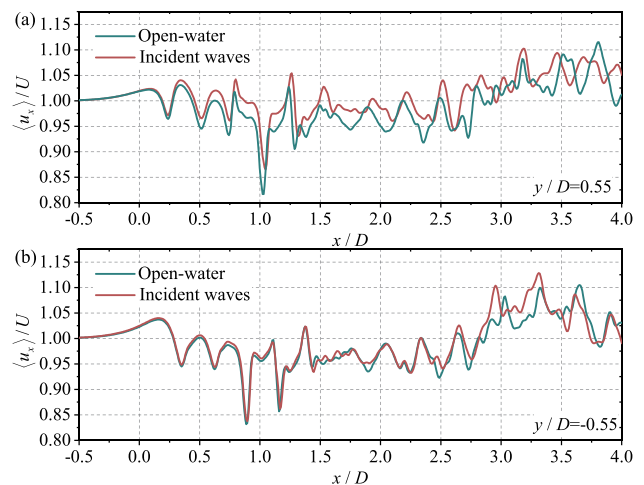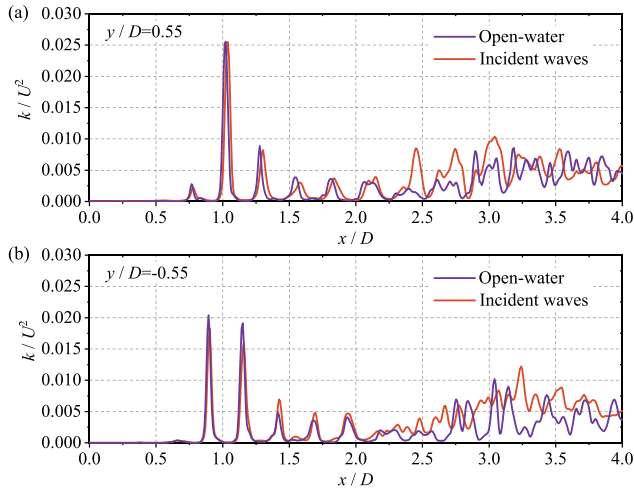

FIG. 11. Phase-averaged axial velocity along the axial direction at the central span of the propeller and at two different elevations: (a) $y/D = 0.55$ and (b) $y/D = -0.55$ for cases under open-water condition and with incident waves.

FIG. 12. Turbulent kinetic energy (TKE) along the axial direction at the central span of the propeller and at two different vertical locations: (a) $y/D = 0.55$ and (b) $y/D = -0.55$ for cases under open-water condition and with incident waves.
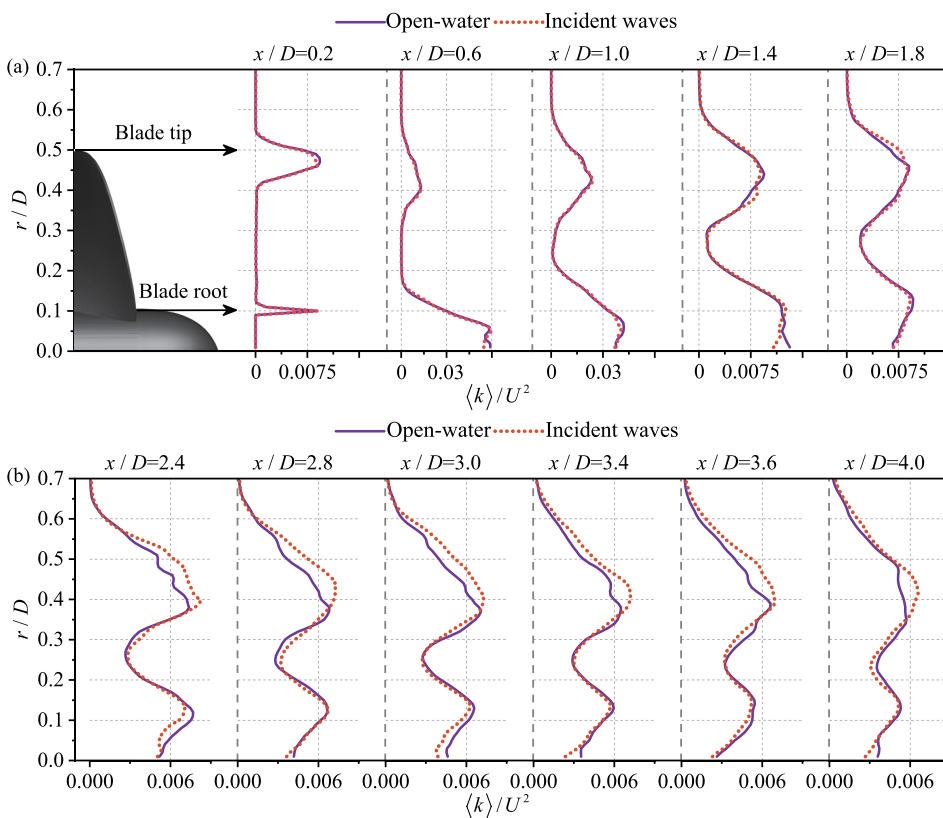
open-water condition and with incident waves. In the near-wake region, the peak TKE occurs quasi-periodically. At $y/D = 0.55$, the presence of waves induces a phase-lag effect on the location of peak TKE, but this effect is not apparent at $y/D = -0.55$. In the far-wake

region, the breakup of the wake vortex makes the flow more irregular, and the quasi-periodical distribution of peak TKE becomes less apparent. Overall, the TKE magnitude with incident waves is larger than that under open-water.

Figure 13 shows the circumferential-averaged radial profile of TKE. In the near-wake region, as shown in Fig. 13(a), the profiles of TKE under the open-water condition and with incident waves are highly consistent. From Fig. 13(b), in the far-wake region, the TKE magnitude with incident waves is larger than that under the open-water condition, particularly between $r/D = 0.35$ and $r/D = 0.55$. This can be attributed to the fact that the wake is less stable in the far-wake region and is therefore more readily disturbed by the effect of waves.

To further analyze the influence of incident waves on the TKE in the propeller wake, we examine the PSD in the frequency space at six monitoring points on the central span. The results for the case with a flat inflow surface are also shown for comparison. Figure 14 shows the locations of these monitoring points. The points are located at three axial locations, $x/D = 0.5$, $x/D = 1.0$, and $x/D = 2.0$, and two radial locations, $r/D = 0$ and $r/D = 0.5$. The time series of velocity were recorded at these points. A fast Fourier transform with a 50% overlapping Hanning window was then applied to obtain the PSD. The results for three operation conditions are compared in Fig. 15.

At all six locations, a region with a slope of $f^{-5/3}$ can be identified, indicating that the turbulent inertial subrange is resolved. This verifies that the present simulations satisfy the requirement of LES. At

FIG. 13. Circumferential-averaged TKE in the (a) near-wake region and (b) far-wake region of the propeller for cases under open-water condition and with incident waves.
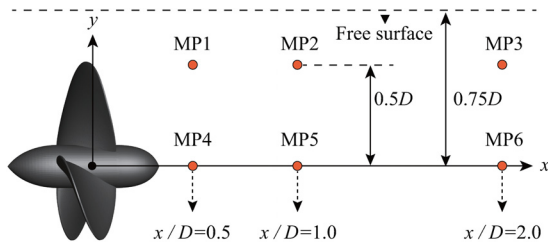
FIG. 14. Monitoring points of the power spectral density (PSD).

points MP1, MP2, and MP3 along the horizontal line $y/D = 0.5$, the energy corresponding to the blade passage frequency f_{blade} is relatively high due to the periodic shedding of tip vortices in all three cases. Compared to the open-water condition, the presence of free surface enhances the energy at frequencies lower than f_{blade}. This enhancement effect is stronger with incident waves than with a flat inflow surface. Among the three monitoring points, the enhancement effect of free surface on the PSD at low frequencies is most significant at MP2, where the water elevation drops under the influence of low pressure (Fig. 9). This phenomenon of an increase in low-frequency energy is related to the energy gained by the propeller wake from the motion of free surface and incident waves. As the wake flows downstream from point MP2 to MP3, the energy enhancement effect shifts to higher frequencies. As shown in Fig. 15(c), the magnitudes of PSD at low frequencies become close to each other for $f < f_{\text{blade}}$ for different cases, whereas the PSD is enhanced because of the presence of free surface at larger frequencies for $f \geq f_{\text{blade}}$. This indicates that there exists nonlinear interaction between the free surface motion and the wake flow, which transports TKE from low frequencies to high frequencies. In contrast to the three points MP1–MP3 close to the water surface, the PSD at the three deeper points MP4–MP6 remains almost unchanged under the influences of free surface.

V. CONCLUSIONS

In the present study, the LES framework was applied to study the turbulent wake of a propeller operating beneath incident waves. The air–water interface and propeller surface were captured using the CLSVOF and IB methods, respectively.

To quantify the effects of incident waves on the turbulent wake, a reference case of a propeller in open-water without incident waves was examined. This case was also used to validate the capability of the present numerical method in capturing the complex geometry of the propeller. Compared with the experimental results, the errors of the LES scheme in the thrust and torque coefficients were found to be less than 5%. The LES also captured the slip-stream contraction phenomenon of the propeller wake.

By comparing the turbulent statistics for cases under the environment of open-water and incident waves, it is discovered that in the near-wake region, the effect of free surface on the mean axial velocity and TKE is confined to the near-surface region. The existence of incident waves leads to acceleration of the wake flow near the water surface. Furthermore, both the mean axial velocity and TKE show a quasi-periodic distribution in the axial direction, and the waves induce a phase-lag effect on their peaks. At larger depths, the effect of waves on the near-wake flow is almost negligible. In the far-wake region, the turbulent wake is destabilized, and the effect of waves on the turbulence statistics becomes more significant. PSD analysis shows that the effect of waves on the TKE is initiated at low frequencies, close to the frequency of the waves. As the wake flows downstream, nonlinear interactions between the wave-induced motion and turbulent fluctuations in the wake transfer energy from low frequencies to high frequencies. As such, the effect of waves on the TKE becomes more significant in the far-wake region.

It should be noted that this paper investigates only the influence of incident waves on the turbulent wakes of a propeller. In the future, the effects of various parameters need to be examined systematically. This includes the ratio of the wavelength to the propeller size, submerging depth, and advance coefficients.
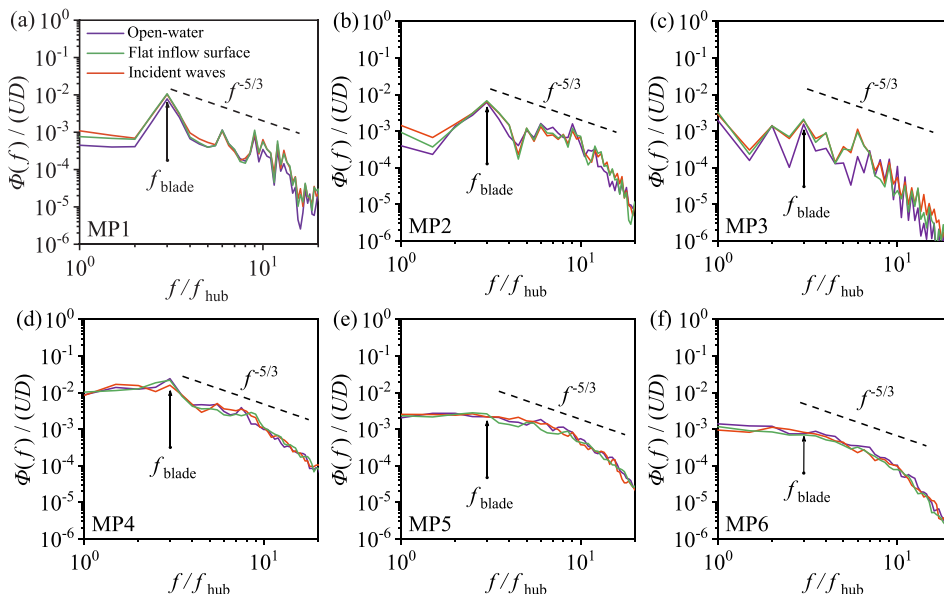
FIG. 15. PSD of kinetic energy at (a) MP1, (b) MP2, (c) MP3, (d) MP4, (e) MP5, and (f) MP6.

AUTHOR DECLARATIONS
Conflict of Interest

The authors have no conflicts to disclose.

Author Contributions

Kan Kan: Conceptualization (equal); Investigation (equal); Methodology (lead); Supervision (lead); Validation (equal); Writing – original draft (equal). **Haoyu Li:** Data curation (lead); Investigation (equal); Validation (equal); Visualization (lead); Writing – original draft (equal). **Zixuan Yang:** Conceptualization (equal); Resources (lead); Software (lead); Supervision (supporting); Writing – review & editing (lead).

DATA AVAILABILITY

The data that support the findings of this study are available from the corresponding author upon reasonable request.

REFERENCES

[1]E. Gungor and U. B. Ozdemir, "Prediction of noise and acoustical spectrum of counter-rotating propellers," J. Ship Res. **62**(03), 166 (2018).

[2]C. Lyu, P. Liu, T. Hu, X. Geng, T. Sun, and R. A. Akkermans, "A sliding mesh approach to the lattice Boltzmann method based on non-equilibrium extrapolation and its application in rotor flow simulation," Aerosp. Sci. Technol. **128**, 107755 (2022).

[3]P. Majumder and S. Maity, "A critical review of different works on marine propellers over the last three decades," Ships Offshore Struct. **18**(3), 391–413 (2022).

[4]L. Wang, T. Wu, J. Gong, and Y. Yang, "Numerical analysis of the wake dynamics of a propeller," Phys. Fluids **33**(9), 095120 (2021).

[5]L. Wang, W. Luo, and M. Li, "Numerical investigation of a propeller operating under different inflow conditions," Phys. Fluids **34**(10), 105118 (2022).

[6]A. Stuermer, J. Yin, and R. Akkermans, "Progress in aerodynamic and aeroacoustic integration of CROR propulsion systems," Aeronaut. J. **118**(1208), 1137–1158 (2014).

[7]S. J. Lee and B. G. Paik, "Stereoscopic PIV measurements of flow around a marine propeller," J. Visualization **7**(1), 25 (2004).

[8]G. Li, Q. Chen, and Y. Liu, "Experimental study on dynamic structure of propeller tip vortex," Pol. Marit. Res. **27**(2), 11 (2020).

[9]M. Felli, D. Di Florio, and F. Di Felice, "Comparison between PIV and LDV techniques in the analysis of a propeller wake," J. Visualization **5**(3), 210 (2002).

[10]M. Felli, F. Di Felice, G. Guj, and R. Camussi, "Analysis of the propeller wake evolution by pressure and velocity phase measurements," Exp. Fluids **41**(3), 441 (2006).

[11]M. Felli, G. Guj, and R. Camussi, "Effect of the number of blades on propeller wake evolution," Exp. Fluids **44**(3), 409 (2008).

[12]M. Felli, R. Camussi, and F. Di Felice, "Mechanisms of evolution of the propeller wake in the transition and far field," J. Fluid Mech. **682**, 5 (2011).

[13]J. Kulczyk, Ł. Skraburski, and M. Zawiślak, "Analysis of screw propeller 4119 using the Fluent system," Arch. Civ. Mech. Eng. **7**(4), 129 (2007).

[14]F. Hong and S. Dong, "Numerical analysis for circulation distribution of propeller blade," J. Hydrodyn. Ser. B **22**(4), 488 (2010).

[15]J. Baltazar, D. Melo, and D. Rijpkema, "Analysis of the blade boundary-layer flow of a marine propeller using a RANS solver," Ocean Eng. **211**, 107633 (2020).

[16]Z. Ren and D. Wan, "Numerical prediction of wall effect on propeller in restricted channel," J. Appl. Math. Phys. **07**(08), 1645 (2019).

[17]A. Stürmer and R. A. Akkermans, "Multidisciplinary analysis of CROR propulsion systems: DLR activities in the JTI SFWA project," CEAS Aeronaut. J. **5**(3), 265–277 (2014).

[18]D. G. Baek, H. S. Yoon, J. H. Jung, K. S. Kim, and B. G. Paik, "Effects of the advance ratio on the evolution of a propeller wake," Comput. Fluids **118**, 32 (2015).

[19]M. Heydari and H. Sadat-Hosseini, "Analysis of propeller wake field and vortical structures using k–ω SST method," Ocean Eng. **204**, 107247 (2020).

[20]B. Ji, X. Luo, X. Peng, Y. Wu, and H. Xu, "Numerical analysis of cavitation evolution and excited pressure fluctuation around a propeller in non-uniform wake," Int. J. Multiphase Flow **43**, 13 (2012).

[21]Y. Long, X. Long, B. Ji, and H. Huang, "Numerical simulations of cavitating turbulent flow around a marine propeller behind the hull with analyses of the vorticity distribution and particle tracks," Ocean Eng. **189**, 106310 (2019).

[22]L. Yao, H. Cao, D. Wu, F. Yu, and B. Huang, "Generation and distribution of turbulence-induced forces on a propeller," Ocean Eng. **206**, 107255 (2020).

[23]X. I. A. Yang, H. H. A. Xu, X. L. D. Huang, and M.-W. Ge, "Drag forces on sparsely packed cube arrays," J. Fluid Mech. **880**, 992–1019 (2019).

[24]J. Hu, Y. Wang, W. Zhang, X. Chang, and W. Zhao, "Tip vortex prediction for contra-rotating propeller using large eddy simulation," Ocean Eng. **194**, 106410 (2019).

[25]P. Kumar and K. Mahesh, "Large eddy simulation of propeller wake instabilities," J. Fluid Mech. **814**, 361 (2017).

[26]S. Ahmed, P. Croaker, and C. J. Doolan, "On the instability mechanisms of ship propeller wakes," Ocean Eng. **213**, 107609 (2020).

[27]C. Wang, P. Li, C. Guo, L. Wang, and S. Sun, "Numerical research on the instabilities of CLT propeller wake," Ocean Eng. **243**, 110305 (2022).

[28]S. Sun, C. Wang, C. Guo, Y. Zhang, C. Sun, and P. Liu, "Numerical study of scale effect on the wake dynamics of a propeller," Ocean Eng. **196**, 106810 (2020).

[29]Q. Zhang and R. K. Jaiman, "Numerical analysis on the wake dynamics of a ducted propeller," Ocean Eng. **171**, 202 (2019).

[30]L. Wang, T. Wu, J. Gong, and Y. Yang, "Numerical simulation of the wake instabilities of a propeller," Phys. Fluids **33**(12), 125125 (2021).

[31]A. M. Kozlowska and S. Steen, "Experimental analysis on the risk of vortex ventilation and the free surface ventilation of marine propellers," Appl. Ocean Res. **67**, 201–212 (2017).

[32]A. Di Mascio, G. Dubbioso, and R. Muscari, "Vortex structures in the wake of a marine propeller operating close to a free surface," J. Fluid Mech. **949**, A33 (2022).

[33]L. Wang, J. E. Martin, M. Felli, and P. M. Carrica, "Experiments and CFD for the propeller wake of a generic submarine operating near the surface," Ocean Eng. **206**, 107304 (2020).

[34]K. J. Paik, "Numerical study on the hydrodynamic characteristics of a propeller operating beneath a free surface," Int. J. Nav. Archit. Ocean Eng. **9**(6), 655 (2017).

[35]C. Guo, D. Zhao, and Y. Sun, "Numerical simulation and experimental research on hydrodynamic performance of propeller with varying shaft depths," China Ocean Eng. **28**(2), 271 (2014).

[36]Y. Li, E. Martin, T. Michael, and P. M. Carrica, "A study of propeller operation near a free surface," J. Ship Res. **59**(04), 190 (2015).

[37]Q. Zhao, C. Guo, Y. Su, T. Liu, and X. Meng, "Study on unsteady hydrodynamic performance of propeller in waves," J. Mar. Sci. Appl. **16**(3), 305 (2017).

[38]W. Zhang, N. Ma, X. Gu, and P. Feng, "RANS simulation of open propeller dynamic loads in regular head waves considering coupled oblique-flow and free-surface effect," Ocean Eng. **234**, 108741 (2021).

[39]M. J. Eom, Y. H. Jang, and K. J. Paik, "A study on the propeller open water performance due to immersion depth and regular wave," Ocean Eng. **219**, 108265 (2021).

08 April 2024 03:40:12

[40]Z. Yang, M. Lu, and S. Wang, "A robust solver for incompressible high-Reynolds-number two-fluid flows with high density contrast," J. Comput. Phys. **441**, 110474 (2021).

[41]D. K. Lilly, "A proposed modification of the Germano subgrid scale closure method," Phys. Fluids A **4**(3), 633 (1992).

[42]M. Germano, U. Piomelli, P. Moin, and W. H. Cabot, "A dynamic subgrid-scale eddy viscosity model," Phys. Fluids A **3**(7), 1760 (1991).

[43]F. Liao, X. Yang, S. Wang, and G. He, "Grid-dependence study for simulating propeller crashback using large-eddy simulation with immersed boundary method," Ocean Eng. **218**, 108211 (2020).

[44]E. Balaras, S. Schroeder, and A. Posa, "Large-eddy simulations of submarine propellers," J. Ship Res. **59**(04), 227 (2015).

[45]A. Posa, R. Broglia, M. Felli, M. Falchi, and E. Balaras, "Characterization of the wake of a submarine propeller via large-eddy simulation," Comput. Fluids **184**, 138 (2019).

[46]A. Posa, R. Broglia, and E. Balaras, "The wake flow downstream of a propeller-rudder system," Int. J. Heat Fluid Flow **87**, 108765 (2021).

[47]I. Borazjani, L. Ge, and F. Sotiropoulos, "Curvilinear immersed boundary method for simulating fluid structure interaction with complex 3D rigid bodies," J. Comput. Phys. **227**(16), 7587–7620 (2008).

[48]K. Kan, Z. Yang, P. Lyu, Y. Zheng, and L. Shen, "Numerical study of turbulent flow past a rotating axial-flow pump based on a level-set immersed boundary method," Renewable Energy **168**, 960 (2021).

[49]M. Wang and P. Moin, "Dynamic wall modeling for large-eddy simulation of complex turbulent flows," Phys. Fluids **14**(7), 2043 (2002).

[50]M. Sussman and E. G. Puckett, "A coupled level set and volume-of-fluid method for computing 3d and axisymmetric incompressible two-phase flows," J. Comput. Phys. **162**(2), 301–337 (2000).

[51]H. S. Howard, "The David W. Taylor model basin," J. Appl. Phys. **15**(3), 227 (1944).

[52]S. D. Jessup, "An experimental investigation of viscous aspects of propeller blade flow," Ph.D. thesis (The Catholic University of America, 1989).

[53]J. Hunt, A. Wray, and P. Moin, "Eddies, streams, and convergence zones in turbulent flows," in *Proceedings of the Summer Program* (Center for Turbulence Research, 1988), pp. 193–208.

08 April 2024 03:40:12